



Water Resources Research

RESEARCH ARTICLE

10.1029/2018WR022823

Key Points:

- Exchange with less-mobile porosity can be directly quantified with the new interface-scale geoelectrical methodology and analysis techniques
- Even high permeability sand and gravel lakebed sediments host less-mobile transport processes with residence timescales of approximately 1 hr
- Direct evidence of anoxic microzone functionality is shown using reactive tracers paired with the geophysical experiments

Supporting Information:

- Supporting Information S1

Correspondence to:

M. A. Briggs,
mbriggs@usgs.gov

Citation:

Briggs, M. A., Day-Lewis, F. D., Dehkordy, F. M. P., Hampton, T., Zarnetske, J. P., Scruggs, C. R., et al. (2018). Direct observations of hydrologic exchange occurring with less-mobile porosity and the development of anoxic microzones in sandy lakebed sediments. *Water Resources Research*, 54. <https://doi.org/10.1029/2018WR022823>

Received 23 FEB 2018

Accepted 19 MAY 2018

Accepted article online 30 MAY 2018

Direct Observations of Hydrologic Exchange Occurring With Less-Mobile Porosity and the Development of Anoxic Microzones in Sandy Lakebed Sediments

Martin A. Briggs^{1,2} , Frederick D. Day-Lewis¹ , Farzaneh Mahmood Poor Dehkordy^{1,2} , Tyler Hampton³ , Jay P. Zarnetske³ , Courtney R. Scruggs¹, Kamini Singha⁴ , Judson W. Harvey⁵ , and John W. Lane¹ 

¹Hydrogeophysics Branch, U.S. Geological Survey, Storrs, CT, USA, ²Department of Civil and Environmental Engineering, University of Connecticut, Storrs, CT, USA, ³Department of Earth and Environmental Sciences, Michigan State University, East Lansing, MI, USA, ⁴Colorado School of Mines, Hydrologic Science and Engineering Program, Golden, CO, USA, ⁵Water Cycle Branch, U.S. Geological Survey, Reston, VA, USA

Abstract Quantifying coupled mobile/less-mobile porosity dynamics is critical to the prediction of biogeochemical storage, release, and transformation processes in the zone where groundwater and surface water exchange. The recent development of fine-scale geoelectrical monitoring paired with pore-water sampling in groundwater systems enables direct characterization of hydrologic exchange between more- and less-mobile porosity during tracer tests. We adapt this technique to sandy interface sediments at a groundwater flow-through kettle lake. Tracer experiments were conducted within controlled-head permeameters over a range of specified downward flow conditions over several days. Although the bed was predominantly composed of highly permeable sands and gravels, cobble inclusions created less-mobile flow zones at the centimeter scale. Less-mobile porosity fractions, residence times, and rates of exchange were inferred from paired bulk and fluid electrical conductivity data, without the need for inverse model calibration. The conservative solute experiments were paired with $^{15}\text{NO}_3^-$ and other reactive amendments, revealing anaerobic processes occurring at shallow sediment depths where pore-water sampling indicated bulk-oxic conditions. The average less-mobile porosity residence times as evaluated with the geoelectrical method were on 1-hr timescales, which appear to be biogeochemically important in the context of creating anoxic microzones within less-mobile porosity of sandy interface sediments.

Plain Language Summary Streams and lakes often exchange water with shallow aquifers, and this exchange can greatly alter water quality and impact greenhouse gas production. Water flows through the shallow sediments that separate surface and groundwater at varied rates due to sediment heterogeneity. However, existing fluid sampling methods typically only sense water moving through the faster pathways, and less-mobile pore spaces are not visible. We present a method to directly measure varied flow rates and residence time within porosity that is less mobile compared to faster flowpaths. The method is applied to a natural lakebed where surface water and groundwaters exchange and indicates that less-mobile porosity may be influential to the transport of nutrients and contaminants.

1. Introduction

Preferential flow through heterogeneous sediments is a universal phenomenon in hydrogeology across spatial scales. In the domain where groundwater (GW) and surface water (SW) exchange, the spatial patterning of dominant advective pathways is largely controlled at the reach-scale by underlying geologic structure and river corridor hydrodynamics (Cardenas, 2004; Gomez-Velez et al., 2015; Payn et al., 2009; Rosenberry et al., 2016; Winter et al., 1998). At the geomorphic unit-scale, extreme preferential flow is accommodated by macropores through low-permeability bed sediments (Menichino et al., 2014), particularly in wetland settings (Hare et al., 2017; Harvey et al., 1995; Lowry et al., 2007). At the pore scale (e.g., Kessler et al., 2014), preferential flow has long been referred to in the aquifer literature as “mobile porosity” (van Genuchten & Wierenga, 1976) and is functionally different from interconnected “immobile” or “less-mobile” porosity.

“Less-mobile” is a relative term, and local flow variations or interdomain diffusion may dominate the bulk mass-transfer timescale between mobile and less-mobile domains (α, T^{-1}) at variable advective water flux rates (Li et al., 1994; McKenna et al., 2001). Less-mobile exchange may be dominated by a range of

©2018. American Geophysical Union.

All Rights Reserved.

This article has been contributed to by US Government employees and their work is in the public domain in the USA.

diffusive (Haggerty, 2004; Haggerty et al., 2001) and/or slow advective (Li et al., 1994; Wheaton & Singha, 2010; Zinn & Harvey, 2003) exchange timescales, which can result in late-time tailing behavior during contaminant transport (Harvey & Gorelick, 2000). Whether exchange between the more- and less-mobile domain is controlled by slow advection or diffusion, at some reduced advective flux, there will be a convergence of mobile and less-mobile pore exchange timescales within the flow system, which would then function as a single effective transport domain (Zheng & Wang, 1999). When flow rate is increased, pores that contributed to less-mobile transport at slower velocities may be incorporated into mobile flow, yielding flow-dependent dynamics (Briggs et al., 2015). It then follows that stream and lakebed mobile/less-mobile exchange is sensitive to natural temporal variations in GW/SW exchange rate and direction, which is known to be dynamic, from subdaily to seasonal timescales (Keery et al., 2007; Lautz, 2012; Schmidt et al., 2011). The phenomenon of “effective” porosity, or the mobile fraction of saturated sediment that directly contributes to advection (McWhorter & Sunada, 1977), is commonly utilized in GW/SW characterization to convert measured volumetric fluxes of water to a flowpath residence time. Less-mobile porosity dynamics are not often explicitly incorporated into models of reactive transport in sediment/water interface (SWI) sediments (Briggs et al., 2015), even though the concept of effective porosity is often invoked.

SWIs are known to possess large gradients in redox zonation relative to surface and subsurface ecosystems (Boano et al., 2014). The role of less-mobile porosity may be particularly influential to redox-sensitive processes (Wondzell, 2015), such as nutrient transformation and greenhouse gas production, because reaction-limited oxic and transport-limited reduced conditions may exist in close spatial proximity. Researchers have harnessed advances in numerical modeling of reactive processes to better predict how interface sediment redox zonation will vary over time in response to variable stream velocity and bed permeability (Bardini et al., 2012) and specifically how this zonation influences reactive nitrogen (N) uptake (Marzadri et al., 2012). However, conceptual approaches that assume distinct thresholds (e.g., time or dissolved oxygen concentration) for flowpath scale anaerobic transitions cannot explain anomalous anaerobic-process signatures that have been observed in bulk-oxic sediments for decades (e.g., Harvey et al., 2013; Holmes et al., 1996; Zarnetske et al., 2011). Variations in local sediment carbon availability (Sawyer, 2015) and pore scale connectivity (Briggs et al., 2015) may create anoxic microzones within bulk oxic sediments. It is hypothesized that less-mobile pore-scale anoxic zones embedded within more mobile, oxic, sediment water may make an important contribution to reactive N uptake (denitrification) and nitrous oxide emission in heterogeneous interface sediments.

An important GW/SW exchange interface occurs between regional aquifers and GW flow-through kettle lakes. In sand-and-gravel coastal glacial-outwash deposits, flow-through lakebeds can process large fractions (e.g., 25%) of total aquifer discharge to the coast (Walter & Masterson, 2002). As kettle lakes typically have no surficial tributaries, there is GW inflow through upgradient lakebed sediments and downwelling through sediments on the opposite side of the lake, creating a “lake shadow” of chemical influence on the downgradient aquifer. Nutrient uptake can be particularly strong in interface sediments due to a labile dissolved organic carbon supply and other reactants that may not exist at depth in the regional sand and gravel aquifer (e.g., Stoliker et al., 2016). Therefore, the reactive interface of downwelling kettle pond sediments is critical to quantify in the context of reactive N transport. The magnitude and direction of downwelling lake-water flux will change seasonally with variation in lake stage (Winter et al., 1998) and over short-term seiche events (Rosenberry et al., 2013). Less-mobile zones proximal to flow obstructions may control development of anoxic microzones in highly permeable glacial sediments where they might not be expected (Dehkordy et al., 2018).

The design of repeatable field experiments to measure multiple porosity domains has been notoriously difficult using solute tracers and fluid sampling alone, because less-mobile exchange parameters are almost exclusively inferred from a mobile-porosity tracer-concentration history over longer flowpaths (1 to 1×10^2 m). These inherently indirect experiments can be sensitive to experimental duration (Haggerty, 2004; Haggerty et al., 2001) and experimental spatial scale (Guan et al., 2008). A balance between flowpath length (advective timescale) and exchange timescales is needed to achieve optimal less-mobile parameter sensitivity in experiments, as illustrated by experimental flowpath Damkohler considerations, using fluid tracer concentration histories alone (Bahr & Rubin, 1987; Wagner & Harvey, 1997). However, this Damkohler concept requires some a priori knowledge of the dominant exchange timescales in field porous media. Further, if a range of advective flux conditions is considered, the experimental flowpath length would also need to scale

with advective rate to maintain the Damkohler balance between mass transfer and advection. Therefore, it has been challenging to confirm in the field the flow-dependent less-mobile exchange dynamics that have been numerically simulated (Li et al., 1994) or indicated in the laboratory (Bajracharya & Barry, 1997) for decades.

Building directly on the geoelectrical observations of mass transfer between mobile and less-mobile domains (Day-Lewis & Singha, 2008; Singha et al., 2007; Swanson et al., 2012), Briggs et al. (2013) presented a framework to analyze paired bulk sediment geoelectrical and fluid electrical conductivity (EC) time series to discern exchange parameters at a scale local to the bulk electrical measurements. This scale is controlled by experimental electrode spacing, which can be reduced in distance to centimeter. Briggs et al. (2013) also introduced a “local” Damkohler number for which the relevant experimental timescale balance is between mass transfer and experimental duration, without a need to consider flowpath length, as less-mobile tracer dynamics are sensed directly within the zone of bulk EC measurement. This approach breaks the dependence on flowpath-scaled experiments and has been successfully applied to field solute injections and controlled laboratory column experiments (Briggs, Day-Lewis, et al., 2014).

We hypothesize that less-mobile exchange in these biogeochemically important kettle-lake sediments is particularly sensitive to flow conditions, because the outwash kettle-pond porous media consists of fundamentally well-connected pores and is therefore dominated by advective flow process over diffusion. To test this hypothesis, we quantify mobile and less-mobile porosity conditions under controlled field conditions with permeameter-scale solute injections into lakebed sediments. We monitor the geoelectrical response (fluid and bulk EC) during tracer breakthrough and quantify less-mobile exchange parameters. Reactive tracers (nitrogen-based) are added to evaluate general redox zonation with depth as well as the presence and function of anoxic microzones within the shallow bulk-oxic region. Here, for the first time in the field, we apply new geoelectrical methods coupled to reactive tracers to reveal functionally different porosity domains in SWI sediments.

2. Methods

Fine-scale geoelectrical measurements paired with pore-water electrical-conductivity time series are used during conservative conductive-tracer additions (NaCl) to quantify physical exchange between mobile and less-mobile porosity. Reactive tracers are used to test for anaerobic processes embedded in bulk-oxic lakebed sediments.

2.1. Field Site

Controlled injections were performed within the SWI of Snake Pond in Sandwich, MA, USA from 6 July to 10 July 2016. Snake Pond is a GW flow-through kettle lake embedded in glacial outwash sands and gravels and without surface tributaries (shown in Figures 1 and 2 of Walter & Masterson, 2002). The lake is situated near the GW high for the large Sagamore lens of the Cape Cod aquifer and therefore characterized by relatively low total dissolved solids. However, historic aviation-fuel pipeline leakage, military ordnance-related compound deposition, and septic system failure have caused concern for contaminant transport through the lake system (LeBlanc, 2003; Walter & Masterson, 2002). GW generally discharges to the lake through the northern, shallow, lakebed sediments and recharges back to the aquifer along the southern shoreline. The injection experiments occurred on the southern, aquifer-recharging shoreline.

Previous work has indicated that the magnitude and orientation of flowpaths between GW and Snake Pond are strongly controlled by shallow sediment connectivity and lake stage (Walter & Masterson, 2002). Seepage patterns of high temporal resolution collected in nearby Ashumet Pond, another flow-through kettle lake, vary in response to short-term rain events of <0.01 m (Rosenberry et al., 2013). It is expected that such changes in flow rate, or direction, within heterogeneous sediments will control the assemblage of less-mobile porosity zones that develop proximal to larger inclusions in the porous media (Briggs et al., 2015; Liu & Kitanidis, 2012). Study of such properties necessitates controlled flow and solute manipulation within approximately 30 cm of the lakebed interface, a shallow region with high biogeochemical reactivity (Harvey et al., 2013; Stoliker et al., 2016). To support the geophysical analysis, sediment core samples were collected in eight streambed locations in the immediate vicinity of the injection experiments. The core

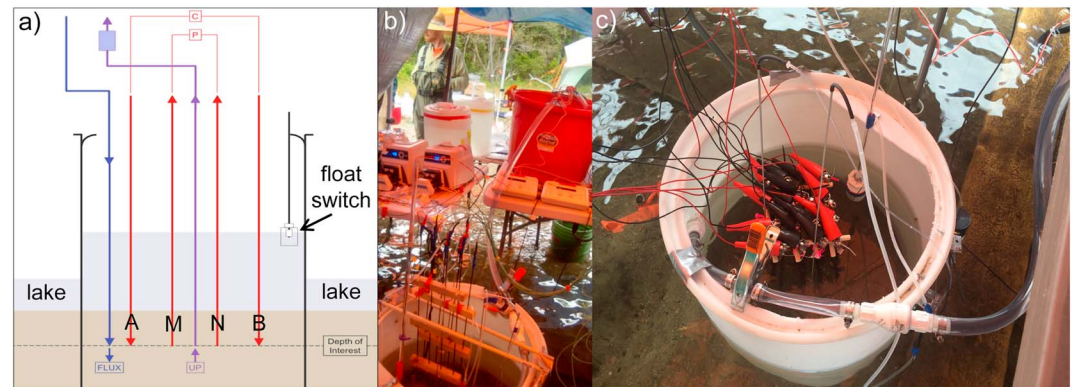


Figure 1. (a) Vertical cross section through the conceptual dual-domain porosity apparatus (DDPA), showing one simplified Wenner electrode array with current (A, B) and potential (M, N) electrodes labeled in red. The dark blue arrows indicate injection discharge into the ring, which was tightly controlled with a float switch to maintain inner ring head above the ambient lake level and enhance natural downwelling patterns. The purple arrow indicates the MINIPOINT-based fluid sampling port installed to a similar distance as the electrode array. (b) Photograph of DDPA1 from above, looking toward the red mediator bucket and other sensing equipment. (c) DDPA2 from above where each of 16 electrodes was connected to the resistivity instrument using alligator clips.

sediments were sieved in the laboratory to determine representative particle size distributions, porosity, dry bulk density, and mean sediment grain size d_{50} (procedures described in Harvey et al. 2013).

2.2. Geoelectrical Characterization of Mobile and Less-Mobile Porosity

Larger scale (m to 1×10^2 -m electrode spacing) arrays of surface electrical-resistivity electrodes have been deployed during conductive tracer tests to spatial map areas of longer-term solute retention at the geomorphic unit scale (Toran et al., 2013; Ward et al., 2010). To facilitate geophysical investigation of less-mobile porosity development and exchange at the centimeter scale in SWI sediments, we developed a methodology to collect paired fluid and bulk EC data in the subsurface during localized constant rate solute injections. Two dual-domain porosity apparatuses (DDPAs) were constructed and installed into the interface sediments to a depth of 0.22 m, approximately 3 m from the southern wetted shoreline (Figure 1). The DDPA consists of an open-ended plastic cylinder (0.55 m diameter) that is inserted in the sediments with a precisely controlled (via small float switch) inner water level (Figure 1a; Text S1 in the supporting information). This water level is maintained at a prescribed height above the local lake stage to drive a consistent downward flux of an electrically conductive (i.e., NaCl) tracer at varying concentrations. Tracer breakthrough is monitored at two depths within the DDPA ring with electrical resistivity arrays (Wenner) and paired fluid EC sampling ports similar to that used for the USGS MINIPOINT discrete-sampling system (Harvey et al., 2013). A fundamental assumption of this method is that the volume of sediments to which a bulk resistivity measurement is most sensitive is coincident in space and comparable to a paired fluid EC point measurement. The resistivity measurement volume also must be small enough to be insensitive to changes in fluid EC within the overlying water column. For this study, the goal of each resistivity array was a constant spacing of 0.05 m, but due to the emplacement of shallow gravels and cobbles, actual electrode spacing varied between 0.04 and 0.07 m. The geometric factor used to determine apparent bulk EC from measured resistance was calculated for each resistivity array using the adjusted electrode distances as described in Text S1. Bulk EC was calculated as the reciprocal of bulk apparent resistivity and converted to $\mu\text{S}/\text{cm}$ for comparison to the fluid EC data. Although fluid specific conductance data (corrected to 25°C) was collected automatically by the flow cells during the field experiments, this record was converted back to uncorrected fluid EC to make the two signals more comparable during sediment temperature changes in order to quantify the less-mobile/mobile porosity fraction (β) using fluid/bulk EC hysteresis patterns.

The pore-scale numerical simulations of Liu and Kitanidis (2012) illustrated a need to conduct experiments regarding less-mobile parameters over a range of flow velocities. Accordingly, our experiments include controlled lakebed injections over a range of downward flux conditions similar to those observed in

Table 1
The Experimental Injection Details for the Coupled Reactive and Conservative Tracers at Location DDPA1 and the Multiflow Conservative Tracers at Location DDPA2

Injection ring	Starting time	Injection flux rate (m/day)	Approx. injection fluid EC ($\mu\text{S}/\text{cm}$)	Reactive tracer flux
DDPA1	9:37 on 7 July 2016	1.2	500	n/a
DDPA1	10:15 on 7 July 2016	1.2	500	K^{15}NO_3 87 $\mu\text{mol N}/\text{hr}$
DDPA1	20:35 on 7 July 2016	1.2–1.4	500	KNO_3 2,590 $\mu\text{mol N}/\text{hr}$
DDPA1	17:10 on 8 July 2016	1.4	500	NaAcO 2,780 $\mu\text{mol C}/\text{hr}$
DDPA1	16:10 on 9 July 2016	1.45	200	NaAcO 7,720 $\mu\text{mol C}/\text{hr}$
DDPA1	15:15 on 10 July 2016	0.9	200	NaAcO 7,720+ $\mu\text{mol C}/\text{hr}$
DDPA2	10:00 on 7 July 2016	1.0	540	n/a
DDPA2	10:30 on 8 July 2016	3.0	1,850	n/a
DDPA2	10:00 on 9 July 2016	5.0	3,670	n/a
DDPA2	17:30 on 9 July 2016	0.9	320	n/a

nearby flow-through kettle lakes and sand-and-gravel-bed rivers (Rosenberry et al., 2013, 2016). Preliminary experimentation at Snake Pond in June 2016 using a DDPA at a fixed injection flux indicated that the experimental shoreline sediments have an average hydraulic conductivity of 10 m/day. Therefore, for the main experiments presented here, the desired injection flux rates (Darcy flux) within the DDPA sediments were obtained by adjusting the float switch to achieve a stable change in head within the cylinder above the pond surface. The targeted head results in a controlled downward hydraulic gradient, assuming purely vertical flow to the bottom of the cylinder at 0.22 m sediment depth and hydraulic conductivity of 10 m/day. Injection flux rates were also spot checked over the course of the experiment by timing known volumes of water passing through a mediator reservoir and dividing by the injection cylinder surface area (0.237 m²).

Two experimental DDPA cylinders were installed: DDPA1, with a relatively steady injection rate, and DDPA2, with variable injection rates. The primary goal of DDPA1 was to assess repeatability of estimates of less-mobile exchange parameters during tracer injection and flush at one advective condition. This multiday experiment was paired with reactive tracers as described below, where flow rate was reduced in a final stage following the completion of geoelectrical experimentation (Table 1). The goal of DDPA2 was to assess the sensitivity of less-mobile exchange parameters to a range of advective conditions. The solute injection was monitored at two depths in DDPA1 (0.095 and 0.145 m) with independent sets of four electrodes and a fluid port at each depth. DDPA2 had 16 electrodes distributed in a grid and two fluid ports at 0.1-m depth within the electrode configuration; the additional electrodes were used to investigate the fine-scale spatial distribution of bulk EC in addition to the less-mobile porosity experiments, so results from only one array are reported here.

The DDPA1 injection was initiated at 1.2 m/day on 7 July 2016, and although the inner-ring head was held steady, a naturally occurring drop in ambient lake level caused a coincident increase in the DDPA1 injection rate from 1.2 to 1.45 m/day by 9 July 2016. The initial 1.2-m/day injection rate was labeled with fluid EC of approximately 500 $\mu\text{S}/\text{cm}$, and plateau conditions were maintained for 3 days until a flush phase with water at approximately 100 $\mu\text{S}/\text{cm}$ that decreased in EC over time (Table 1). The DDPA2 injection began at 1 m/day on 7 July 2016, was increased to 3 m/day on 8 July 2016, was increased again to 5 m/day on 9 July 2016, and finally was dropped down to 0.9 m/day later on 9 July 2016. Although the 5-m/day flux is well above the maximum observed in nearby natural systems (e.g., approximately 3 m/day), this strong injection was performed to explore a high-flow rate end member. These four stepwise adjustments in downward flux through the DDPA were labeled with injection water EC of approximately 540 (1 m/day), 1,850 (3 m/day), 3,670 (5 m/day), and 320 $\mu\text{S}/\text{cm}$ (0.9 m/day), respectively (Table 1).

2.3. Reactive Tracer Injections and Analyses

A total of five reactive tracer experiments were paired with the geoelectrical experiments of DDPA1. These experiments were designed to assess various limited factors on SWI-sediment nitrogen (N) reactivity and directly test for anaerobic processes occurring in bulk-oxic zone. Following Marzadri et al. (2014), we

operationally define bulk oxic conditions as pore water with $>62.5 \mu\text{mol O}_2/\text{L}$. The limiting reactant analysis is not discussed here in detail, as we focus on indicators of anoxic microzones in sediments that show dissolved oxygen in mobile pore water. The first four injections occurred during the multiday flux rate that was held in the range of 1.2 to 1.45 m/day, and an additional injection occurred on 9 July 2016 at a reduced flux rate of 0.9 m/day. K^{15}NO_3 was used to label ambient reactive N process at similar bulk N levels, while KNO_3 raised bulk reactive N concentrations. NaAcO (acetate) was used to increase labile C concentrations above a background. The reactive injections proceed sequentially as indicated in Table 1.

Porewater sampling (using a MINIPPOINT system) for isotope and solute conditions during the injections was accomplished using a closed peristaltic pumping system. The water was pumped directly into cleaned, sealed, sampling syringes. The water samples for all nongas samples were then immediately filtered in series through a $0.7\text{-}\mu\text{m}$ glass-fiber filter and $0.2\text{-}\mu\text{m}$ cellulose acetate filter into acid-washed amber Nalgene bottles. Samples were taken in triplicate from SW and the 0.095- and 0.145-m depths for each of the five experiments. Real-time dissolved-oxygen data were sampled from each depth using in-line flow-through cells equipped with fiber-optic oxygen microsensors attached to a FireStingO2 Optical Oxygen Meter (Pyro Science, Germany). Water samples for NO_3^- and $^{15}\text{NO}_3^-$ were chilled on site following collection and preserved at 4°C until analyzed. For the dissolved gas samples, 1.5875-mm outside diameter tubing directly from the pump was placed into the bottom of a 12-mL Labco glass exetainer, and water was allowed to overflow the exetainers by an additional full volume.

These gas samples were preserved with $120 \mu\text{L}$ of 50% w/v ZnCl solution before being sealed with zero head-space. Gas samples were stored at room temperature in the dark and later shipped to the Stable Isotope Facility (SIF) at the University of California-Davis, for isotope (^{15}N) analysis of dissolved gases (N_2 and N_2O). In less than 6 hr from sampling, all water samples were separated into groups for ^{15}N analysis of NO_3^- , which were frozen, then shipped frozen to Stable Isotope Facility. Stable isotope ratios of nitrogen (^{15}N) in gas were measured using a ThermoScientific GasBench + Precon gas concentration system interfaced to a ThermoScientific Delta V Plus isotope-ratio mass spectrometer (Bremen, Germany). Nitrate in water samples were converted to N_2O by bacteria denitrification assay, and ^{15}N ratios were measured as stated above. NO_3^- concentrations were measured by a Dionex ICS-2100 Ion Chromatography System (ThermoScientific) at Michigan State University.

2.4. Semianalytical Quantification of Less-Mobile Porosity Exchange Timescales

Briggs, Day-Lewis, et al. (2014) presented analytical and semianalytical models to estimate less-mobile porosity parameters based on collocated measurements of bulk and fluid EC. Here we summarize the semianalytical approach (presented in section 3.1.3 of Briggs, Day-Lewis, et al. (2014) with minor modifications), and we use this approach to estimate alpha (α, T^{-1} , the “classic” mass transfer rate as defined by Ma and Zheng, 2011).

Assuming the bicontinuum Archie model for the bulk conductivity of a dual-domain medium (e.g., Singha et al., 2007),

$$\sigma_b = (\theta_m + \theta_{lm})^{q-1} (\theta_m \sigma_m + \theta_{lm} \sigma_{lm}) \quad (1)$$

where σ_b is the measured bulk EC, θ_m is the mobile porosity, σ_m is the mobile porosity EC, θ_{lm} is the less-mobile porosity, σ_{lm} is the less-mobile porosity EC, and q is the cementation exponent (assumed to be 1.7 for this work). Experimentally, it is possible to measure σ_m using fluid sampling. If the time series of σ_m (as it approaches equilibrium with the tracer injection concentration) can be approximated by a differentiable function, for example, a second-order polynomial, we can rewrite equation (1) as follows:

$$\sigma_b = (\theta_m + \theta_{lm})^{q-1} [\theta_m (at^2 + bt + c) + \theta_{lm} \sigma_{lm}] \quad (2)$$

where a , b , and c are polynomial coefficients.

Differentiating with respect to time, we get

$$\frac{\partial \sigma_b}{\partial t} = \theta_m (\theta_m + \theta_{lm})^{q-1} (2at + b) + \theta_{lm} (\theta_m + \theta_{lm})^{q-1} \frac{\partial \sigma_{lm}}{\partial t} \quad (3)$$

Substituting the transport equation for less-mobile concentration for $\frac{\partial \sigma_{lm}}{\partial t}$, we obtain

$$\frac{\partial \sigma_b}{\partial t} = \theta_m (\theta_m + \theta_{lm})^{q-1} (2at + b) + \alpha (\theta_m + \theta_{lm})^{q-1} (\sigma_m - \sigma_{lm}) \quad (4)$$

Solving equation (2) for σ_{lm} , substituting for that quantity, and substituting the polynomial expression for σ_m yields the single ordinary differential equation

$$\frac{\partial \sigma_b}{\partial t} = (\theta_m + \theta_{lm})^{q-1} \left\{ \theta_m (2at + b) + \alpha \left[at^2 + bt + c - \left(\frac{\sigma_b / (\theta_m + \theta_{lm})^{q-1} - \theta_m (at^2 + bt + c)}{\theta_{lm}} \right) \right] \right\} \quad (5)$$

Equation (5) has a simple analytical solution, although it is unwieldy and hence not shown here. Initial conditions for bulk and fluid conductivity are identified experimentally, and equation (5) is fit to data using non-linear regression to identify the best-fit α . As stated above, this approach is based on the semianalytical model of Briggs, Day-Lewis, et al. (2014), with the minor modification that a polynomial function is used to approximate σ_m and the derivative of that function also is used.

3. Results

Results from the geoelectrical characterization of paired mobile and less-mobile porosity dynamics are presented below along with the reactive tracer findings.

3.1. Geophysical Experiments

The d50 across all lakebed cores is 0.5 mm (standard deviation 0.09 mm), characteristic of medium to coarse sands, and little particulate organic matter content was found below the SWI. Pebbles and cobbles (≥ 4 mm with occasional cobbles exceeding 60 mm; Figure 2a) were regularly encountered during DDPA installation; however, they were removed from sieve analysis with the purpose of characterizing the primary granular texture. Discrete depth sampling indicated a coarsening of material with depth over the upper 0.1 m. Porosity of these segments ranged from 0.27 to 0.35 with a mean of 0.3; pebbles and cobbles larger than 20 mm were neglected from this porosity analysis by necessity.

Fluid and bulk EC data described in this study are available in Briggs et al. (2018). During tracer injection, fluid and bulk EC breakthrough curves from 0.145 m show simultaneous initial change from background (Figure 2b), indicating collocation of fluid and bulk EC measurements. Additionally, the bulk EC measurement was insensitive to early changes in the overlying water column fluid EC, indicating the electrode spacing was appropriate for shallow bed-sediment characterization; that is, bulk EC measurements are not affected by the water column. After initially changing together, the shapes of the bulk and fluid EC rising and falling limbs diverge for a period of time, indicating delayed pore water EC change in less-mobile porosity relative to mobile water reflected in the collocated fluid EC record (Figure 2b). When plotted in fluid/bulk EC concentration space, the resulting hysteresis pattern shows approximate mirror symmetry, indicating that similar less-mobile exchange processes were observed during the enrichment and flush phases of the injection experiment (Figure 2c). This symmetry also suggests that the electrical averaging of mobile and less-mobile fluid EC components of bulk EC appears approximately arithmetic (Day-Lewis et al., 2017), a basic assumption of the graphical less-mobile exchange parameter analysis techniques presented by Briggs, Day-Lewis, et al. (2014) and utilized here. Due to incomplete tracer replacement in the overlying water column during the flush injection phase, the hysteresis loop closes at a more conductive point than the background porewater condition and continues to drop slowly at late time (Figure 2c). This latter rate of EC change was clearly slower than the time-scale of less-mobile porosity exchange, shown by the linear relationship between fluid and bulk EC along the equilibrium best-fit line, as would be predicted by Archie's Law in the absence of mass transfer (Archie, 1942).

Using the experimental hysteresis, the parameter β , or the ratio of less-mobile/mobile fractions of total porosity, was estimated graphically as described in detail by Briggs, Day-Lewis, et al. (2014) and shown in Figure 2c by projecting hysteresis hinge points. Based on Day-Lewis et al. (2017), we expect the falling limb to conform more closely to the arithmetic-averaging (parallel conduction) assumption underlying the graphical analysis; hence, we focus on that limb first (Figure 3). Considering the linear portion of the falling limb (i.e., bulk EC > 25 $\mu\text{S}/\text{cm}$), β was determined by linear fit to be 0.97 and by least-squares linear

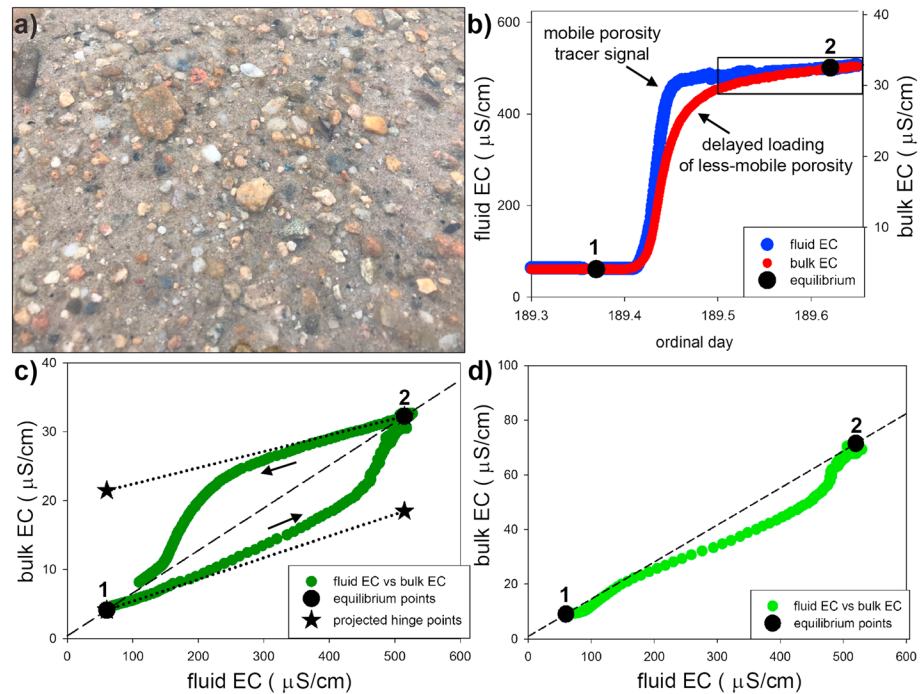


Figure 2. (a) Image of typical Snake Pond sand and gravel interface sediments where the largest cobbles are approximately 6 cm across. (b) Bulk and fluid EC tracer response from 0.145-m depth in DDPA1 temporarily diverge, characteristic of delayed loading of less-mobile porosity. (c) A hysteretic relation between bulk and fluid EC with approximate mirror symmetry is shown. The slope of the dashed best-fit line to the two equilibrium points in concentration space is used to estimate total porosity. (d) The rise to tracer injection plateau at the more shallow 0.095-m depth, which shows a more linear relation compared to (c), indicating a reduced fraction of less-mobile porosity.

regression to be 1.03. Considering the rising limb, a regression-based fit to the linear portion of the data (i.e., bulk EC 4.4–7.0 $\mu\text{S}/\text{cm}$) produced an estimate of β of 1.09. These results indicate a near-even balance of mobile and less-mobile pore space within the region of measurement sensitivity. Additionally, the similarity of β extracted independently from rising and falling hysteresis limbs indicates that the approximately 20% increase in flow rate from injection to flush experimental phases did not noticeably impact the less-mobile porosity fraction at this 0.145-m depth in DDPA1.

The cementation exponent of Archie's Law relates fluid and bulk EC at equilibrium conditions based on the connectedness of pore space and can be derived experimentally from this best-fit line and the total porosity of the media; however, it is not possible to quantify both porosity and the cementation exponent simultaneously from fluid and bulk EC. If we assume that the cementation exponent for the Snake Pond sediments is 1.7, consistent with unconsolidated sands and gravels and geophysical evaluation of nearby aquifer material (Singha & Gorelick, 2005), we can use the fluid/bulk EC equilibrium relation (Figure 2c) to estimate the total porosity, yielding a value of 0.2. This value is somewhat less than the range of porosity observed here in the cobble-free sediment cores and likely is influenced by the subsurface cobble encountered during 0.145-m-depth electrode installation—cobbles would serve to reduce total porosity within the electrical measurement volume. Based on the graphical analysis of β (approximately 1.0) and total porosity (0.2), mobile porosity is estimated at 0.1 and less-mobile porosity at 0.1. For data to be appropriate for the semi-analytical α analysis, less-mobile exchange must dominate changes in bulk EC; this condition is satisfied during the late-time injection and flush phases when fluid EC is essentially at equilibrium (Figure 2b inset box; Figure 3). Estimating α independently for the injection and flush breakthrough curves yields similar values of 2.74 and 3.23/day (Figures 3c and 3d), respectively. These exchange timescales are converted to corresponding mean residence times in the local less-mobile porosity domain by taking the inverse and multiplying by θ_{lm} , yielding values of 53 and 45 min, respectively.

Paired fluid and bulk EC collected at the shallow 0.095-m-depth array in DDPA1 show reduced differential tracer loading, indicated as a departure during the injection phase from the best-fit equilibrium line, indicating

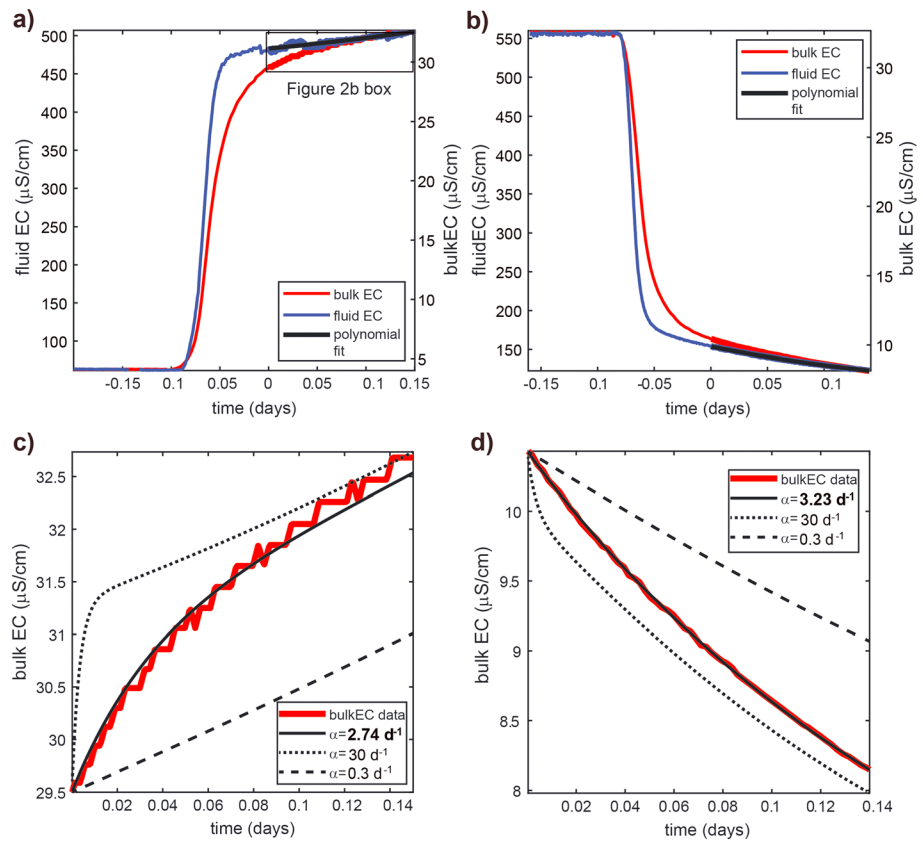


Figure 3. (a) and (b) show late-time injection and flush-phase tracer data that are utilized to determine the characteristic timescale of less-mobile exchange (α) for the rise and flush data at DDPA1 0.145 m. The best-fit α is identified by fitting the bulk electrical conductivity (EC) late-time flush data using the relation presented in equation (5) and the measured mobile and less-mobile porosity fractions independently for the (c) tracer injection and (d) tracer flush, experimental phases.

mobile porosity domain dominance (Figure 2d). This array was installed directly above the 0.145-m-depth array and did not directly encounter cobbles during installation; it is reasonable to assume that this shallower investigation volume is more sand dominated. The interpretation is supported by the bulk EC at tracer equilibrium, which is approximately twice that of the lower array at 70 $\mu\text{S}/\text{cm}$ and indicates higher total porosity (Figure 2d). In sand-and-gravel sediments with high pore-throat connectivity, we may expect the cementation exponent to be similar throughout the material. When a line is fit to initial background and tracer plateau equilibrium points of the shallow array data (Figure 2d), and a cementation exponent of 1.7 again assumed, total porosity is estimated at 0.31, similar to the sediment core average.

As noted earlier, DDPA2 had eight electrode arrays inserted to the 0.1-m depth, though only data from one array is shown here. At this location there is visible separation between the curves at lower injection fluxes with bulk EC lagging fluid EC, but the curves converge in shape at the higher flux rates (Figure 4a). This result qualitatively indicates flow-dependent less-mobile exchange, where the characteristic timescale of exchange is increased at higher flow (faster loading of less-mobile pores). When bulk and fluid EC are plotted together in concentration space, successive “rising” hysteresis limbs are observed at each increased injection fluid EC level, even for the high 5-m/day downward flux rate (Figure 4b). Therefore, although visually the curves more closely align in shape with stronger advection, there is shorter-term delayed bulk EC loading within a large fraction of the experimental volume at all four experimental injection rates. We then conclude that β may be similar over this range of fluid fluxes (0.9–5 m/day), but the effective α is positively related to bulk flow rate. A quantitative graphical analysis of β was not attempted as only half of each hysteresis loop was collected, and the recent pore network modeling of Day-Lewis et al. (2017) indicates that the rising hysteresis limb, when less-mobile zones are more electrically resistive than adjacent mobile spaces, is particularly susceptible to violation of the fundamental arithmetic EC averaging assumption.

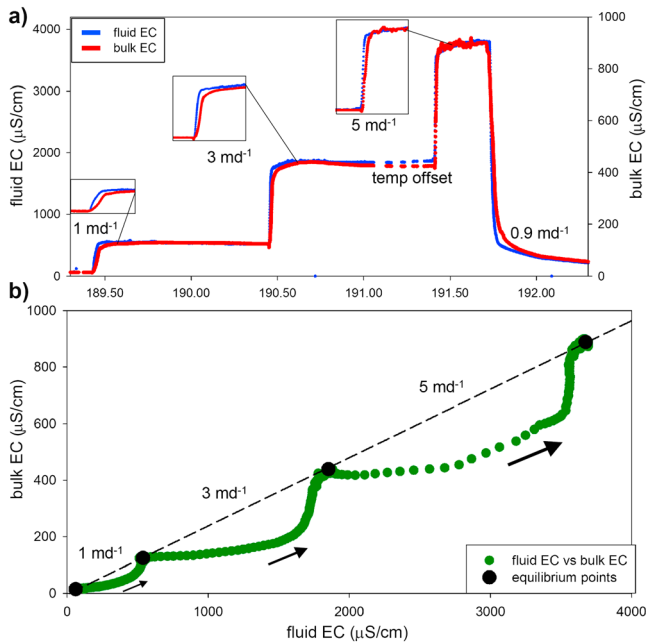


Figure 4. (a) The total fluid and bulk electrical conductivity (EC) time series throughout the four-stage multiflow experiments. The fluid and bulk EC track more closely at higher flow, indicating enhanced exchange between porosity domains. (b) The rising hysteresis limbs for the 1, 3, and 5 m/day experiments, which are similar in shape, indicating that the less-mobile porosity fraction may be similar across these flow rates within the region of measurement. The equilibrium points follow a linear relation as predicted by Archie (1942), and this slope indicates a relatively large total porosity of 0.43.

If a cementation exponent for sands and gravels of 1.7 is again assumed for the sandy DDPA2 sediments, the slope of best fit line to the four bulk/fluid equilibrium points ($r^2 = 0.99$) indicates a large total porosity of 0.43 within this zone of measurement (Figure 4b). As the β calculation was not performed for this data set but a large departure from the Archie-predicted equilibrium line was observed for each injection rate, we assume a less-mobile fraction of 50% to 90% for the purposes of the α calculation. Using these two end-member values for less-mobile porosity of 0.22 and 0.39, a theoretical range for α of 6.7 to 15.2/day was determined for the lowest experimental injection flux of 0.9 m/day (Figure 5).

3.2. Reactive Experiments

As mentioned above, a series of reactive tracer additions were performed in DDPA1 (Table 1) concurrent with the geoelectrical characterization of less-mobile porosity at the 0.145-m depth. Oxygen concentrations remained above $100 \mu\text{mol O}_2/\text{L}$, well above the anoxic threshold of $62.5 \mu\text{mol O}_2/\text{L}$, within DDPA1 during the first three chemical manipulation experiments that took place. However, despite these high O_2 pore water concentrations (bulk oxic sediments), following the addition of the $^{15}\text{NO}_3$ tracer at 5 atom-%, $^{15}\text{N}_2\text{O}$ gas was observed at 0.095- and 0.145-m depths (Figure 6a). Median concentration at 0.095-m depth was $67.5 \text{ pmol } ^{15}\text{N}_2\text{O-N/L}$, and concentrations were higher at 0.145-m depth at $131 \text{ pmol } ^{15}\text{N}_2\text{O-N/L}^{-1}$. The addition of acetate was designed to elicit a response in oxygen uptake rates and cause the anoxic interface to migrate upward toward the sediment surface if reactions were carbon-limited. A vertical shift in the oxygen conditions indeed occur with the acetate addition. Specifically, during the fourth experiment at a higher acetate addition concentration, followed by the fifth experiment with increased residence time, the O_2 concentrations at 0.145 m dropped

below $10 \mu\text{mol O}_2/\text{L}^{-1}$, indicating the bulk anoxic transition had shifted upward to somewhere between the 0.095- and 0.145-m depths (Figure 6b). $^{15}\text{N}_2\text{O}$ concentrations increased at both depths by over 50% for this reduced flux experiment.

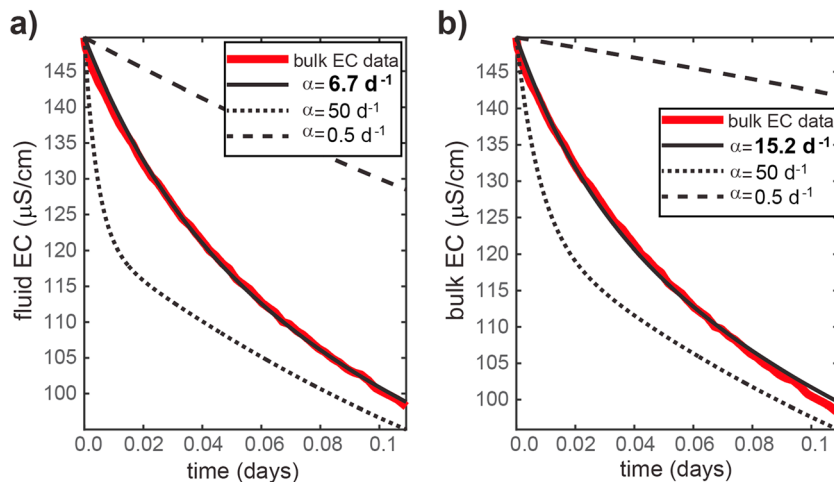


Figure 5. Similar to Figure 2d, these plots show how the best-fit alpha parameter (α) is identified for the DDPA2 location by fitting the bulk electrical conductivity late-time flush data using the relation presented in equation (S5). Total porosity was determined experimentally at 0.43, and we show α fits assuming: (a) less-mobile porosity is 50% of this total, or (b) 90% of this total. For reference, lines for results from an α of 0.5 and 50/day are shown (approximately \pm one order of magnitude).

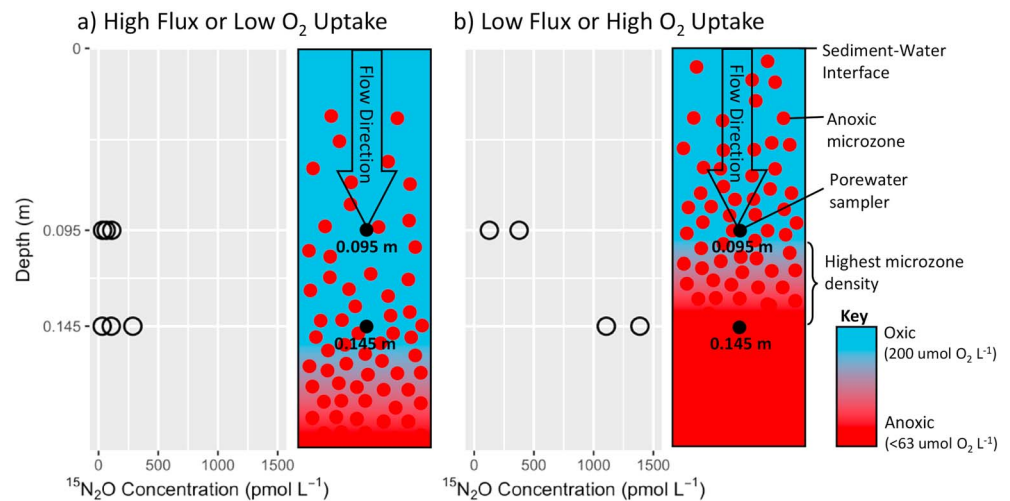


Figure 6. The reactive tracer data from DDPA1 are divided between the first three experiments (a), at a high flux or low O_2 uptake where the entire flowpath remained oxenic ($>100 \mu\text{mol } O_2/\text{L}$), and the latter two experiments (b), where low flux (increased residence time) or high O_2 uptake created increased O_2 consumption ($<10 \mu\text{mol } O_2/\text{L}$ at 0.145-m depth). The plot in (a) shows a positive response in mean $^{15}\text{N}_2\text{O}$ concentrations (denitrification byproduct) measured at the 0.095- and 0.145-m depths. (b) illustrates how the bulk anoxic transition was shifted upward toward the sediment water interface when downward vertical water flux was reduced and dissolved carbon increased.

4. Discussion

Less-mobile residence times on the order of 1 hr appear to drive local-scale anaerobic reactivity at the naturally downwelling lakebed SWI. Changes in downward flow rate directly impact the timescales of less-mobile solute mass transfer, indicating anoxic microzone formation in sand and gravel sediments is a highly dynamic process.

4.1. Exchange With Less-Mobile Porosity

The biogeochemical implications of exchange in systems with less-mobile intragranular porosity has been considered (Kessler et al., 2014), but solid silica-based sand-and-gravel sediments are not an intuitive setting to expect less-mobile dynamics due to high expected fractions of well-connected (effective) porosity. However, when a 3D volume of sediment is considered, flow obstructions within sandy sediments caused by embedded gravels and cobbles may create leeward hydraulic “dead zones” (Dehkordy et al., 2018) that function as less-mobile porosity even though all pore throats are fundamentally large and well connected, consistent with numerical modeling (Briggs et al., 2015; Liu & Kitanidis, 2012). The fraction of less-mobile porosity quantified here for the 0.145-m depth in DDPA1 is substantial with a β of 1, but this is within the lower range observed at other sites with varied tracer methodology. Culkin et al. (2008) observed β equal to approximately 10 in deeper borehole experimentation regarding aquifer storage and recovery dynamics. In near-river sediments in Colorado, Briggs et al. (2013) characterized β ranging from approximately 0.3 to 4. At the complex MADE contaminant transport research site, Feehley et al. (2000) estimated β at 7, whereas Harvey and Gorelick (2000) estimated β at 7, resulting in a much larger less-mobile domain relative to mobile porosity.

SWI sediments are typically quite heterogeneous, ranging from interbedded sands and silts to more poorly sorted grain distributions. Our quantitative less-mobile exchange analysis indicates that the presence of cobbles in the flow field can create downgradient areas of stagnation, similar to boulder obstructions in surface streams. These hydraulic effects are likely to be more dynamic in response to changes in flow rate and direction than less-mobile zones controlled by diffusive solute exchange (e.g., clay lenses). Differential loading of less-mobile pore spaces during controlled perturbations of injection EC as monitored by paired bulk and fluid EC offer the first means we are aware of in situ characterization of these flow-dependent local-scale exchange dynamics.

Whether or not a crystalline cobble is included within the bulk EC measurement volume will strongly impact total porosity of that volume (large cobbles reduce total porosity and bulk EC) and the development of local less-mobile porosity zones. The observed difference in parameters between the deep and shallow arrays indicates that the scale of sediment heterogeneity controlled by cobbles (e.g., Figure 2a) is larger than the volume of sediment investigation supported by 0.05-m electrode spacing. This allows targeting of less-mobile exchange parameters in discrete spatial zones near the SWI that may be influential to reactive processes. However, representative elementary volumes of sediment variability within the injection ring are not captured by this experimental design. Depending on the size of inclusions such as cobbles, or fine-grained lenses in other systems, it may be difficult to evaluate a true representative elementary volume using the small electrode spacing necessary (here approximately 0.05 m) to avoid water column influence on the electrical measurements. In that case, multiple geoelectrical measurements will be needed to more fully characterize SWI less-mobile exchange parameters to be used in predictive contaminant transport modeling.

Paired fluid and bulk EC data from the time period approaching equilibrium tracer conditions are used to determine the characteristic exchange timescales (e.g., α) without the need for inverse model calibration (Figures 3 and 5). The upper limits determined for local residence time in less-mobile porosity zones approach 80 min in DDPA2, using assumed porosity fractions. This local residence timescale decreases at higher flow based on the convergence of fluid and bulk EC tracer signals at the higher 3- and 5-m/day injection flux rates. Quantifying how less-mobile exchange timescales vary with interface flow conditions offers important insights into the physical controls on embedded redox zonation in these downwelling lakebed sediments. For example, at times of high flux rate from SW to GW, there is still differential loading of mobile and less-mobile porosity domains, but the decreased less-mobile residence time will become less influential biogeochemically assuming similar kinetic rates.

The less-mobile residence times evaluated for this 0.145-m depth in DDPA1 are approximately 3 \times longer than that measured in the laboratory using similar methodology for zeolite grains with high internal porosity (Briggs, Day-Lewis, et al., 2014; Swanson et al., 2012). Assuming characteristic anoxic threshold times for porewater biogeochemical processes on the order of hours (e.g., Briggs, Lautz, & Hare, 2014), this local increase in porewater residence time adjacent to cobbles could potentially lead to the formation of anoxic microzones embedded in bulk-oxic SWI sediments. All five reactive tracer experiments conducted in tandem with the geoelectrical experiments in DDPA1 support this by showing anaerobic reaction byproducts at sediment depths where the mobile pore water still contained dissolved oxygen (Figure 6).

4.2. Anoxic Microzones

Reactive processes in pore water are typically limited by the timescales of transport or reaction, and the balance between these is described by various Damkohler numbers (e.g., Zarnetske et al., 2012). Dissolved oxygen consumption can be increased at the local scale in less-mobile porosity of SWI sediments through increased residence/contact time (Briggs et al., 2015). The reduction of NO_3 to N_2O is an anaerobic process, which should be thermodynamically inhibited in oxic conditions (Hedin et al., 1998); however, it has been shown to occur in oxic sediments and is attributed to the presence of undefined anoxic microsites (Harvey et al., 2013; Triska et al., 1993; Zarnetske et al., 2011). Here we also observe accumulation of denitrification byproducts in the fully oxic sediments during our experiments. Previous work has shown that the highest rate of net $^{15}\text{N}_2$ production per flowpath-scale residence time occurs as the bulk anaerobic threshold is approached, but oxygen is still present in mobile pore water (Zarnetske et al., 2011). Considering a local residence time-based framework incorporating less-mobile porosity, the concentration of anoxic microzones would be expected to increase just upgradient of the bulk anaerobic threshold (Figure 6b; Briggs et al., 2015), potentially explaining this hot-moment of denitrification.

The first four experiments conducted at the higher 1.2 to 1.45-m/day downward flux rates show evidence of anoxic microzones, with concentration in reduced ^{15}N increasing with depth in the bulk-oxic zone. As labile carbon availability is enhanced in the fourth experiment (acetate addition), anoxic conditions were approached at the 0.145-m depth in DDPA1, while median residence time to that depth based on the salt tracer flush is only approximately 30 min. When the downward flux rate was reduced for the final experiment to 0.9 m/day, the bulk-anoxic transition shallowed above the 0.145-m depth, and ^{15}N accumulation increased at 0.095 m. Therefore we effectively captured the bulk anaerobic transition between the 0.095- and 0.145-m depths and also provide further evidence for increased microzone concentration just upgradient of this

threshold, as depicted in conceptual Figure 6b. Recent flume bedform-scale research by Kaufman et al. (2017) using planar optode dissolved-oxygen imaging showed that the “transition zone” from bulk oxic to anoxic is wider and more ragged when water flux rate through the bedforms was decreased, and the transition zone contact moves toward the SWI, compared to when flux rates were increased and the transition was pushed deeper. The authors then postulate that these wider dissolved-oxygen transition zones may be mistakenly interpolated as anoxic microsites in previous studies if flux rates are dynamic. While this certainly is plausible for downward advancing redox boundaries expected under enhanced fluid flux rates, the controlled, contracting threshold created here, where greater ^{15}N is observed in shallow sediments known to be oxic over several days prior, offers direct evidence of enhanced microzone functionality just upgradient of bulk redox transitions.

There has been extensive discussion regarding where and when hyporheic exchange is important to downstream nutrient transport. A review of stream transient storage characterizations, where the hyporheic zone is typically modeled as less-mobile compared to in-channel flows, indicated that the ratio of volumetric hyporheic exchange to total stream discharge is often quite small (Wondzell, 2011). However, if reaction rates within transient storage compartments are orders of magnitude higher than the main channel, even relatively small exchange flows may be influential to net chemical change of SW (Stewart et al., 2011). The hyporheic exchange flow ratio concept can be scaled to streambed mobile and less-mobile porosity. We calculate the 1D local less-mobile exchange flux for the 0.145-m depth in DDPA1 of 0.14 m/day by multiplying α (2.74 m/day) by an assumed flowpath length scale (0.05 m), neglecting any effect of tortuosity. When compared to the known initial bulk vertical injection rate of 1.2 m/day, approximately 11% of total flow would be expected to exchange with local less-mobile porosity. The balance between internal residence times (average approximately 1 hr) and reaction timescales within less-mobile zones will then control the potential to form anoxic microsites (Briggs et al., 2015). Assuming similar reaction rates in mobile porosity, the residence time clock “starts” upon injected water passing through the SWI. Average travel time to the 0.145-m depth is 0.8 hr based on the median tracer breakthrough time during the injection phase. Therefore, the additional 1 hr of local less-mobile residence time could be expected to cause a transition to anoxic conditions assuming a threshold time of 1.3–2.3 hr as has been observed in other shallow downwelling sediments (Briggs, Lautz, & Hare, 2014). Further, we show with the reactive acetate experiment that bulk anoxic conditions were approached at the 0.145-m depth with an average flowpath residence time (from the SWI) of only 45 min; so it seems reasonable that local less-mobile residence timescales that average 1 hr have potential to induce anoxia.

Conversion of NO_3^- to the powerful greenhouse gas nitrous oxide is expected to occur under intermediate residence times that yield incomplete denitrification (Firestone & Tiedje, 1979; Quick et al., 2016). Less-mobile porosity-enabled incomplete denitrification facilitated by less-mobile porosity embedded in the bulk oxic zone has the potential to produce nitrous oxide in systems where deeper long-residence time flowpaths would produce inert N_2 gas. This has been indicated here with direct measures of $^{15}\text{N}_2\text{O}$ in the bulk oxic zone under varied experimental conditions. Diffusion with biofilms on grain surfaces is expected to contribute to anaerobic respiration in the bulk-oxic zone of bed sediments. Although in large grained material such as the sands and gravels of Snake Pond, the total volume of pore space occupied by biofilm mass is unlikely to rival the 50% fraction quantified here for the 0.145-m experimental depth. In fine-grained bed sediments with greater total surface area, the net impact of anoxic biofilm exchange may be expected to be more appreciable and even contribute to the formation of less-mobile porosity zones through pore clogging.

5. Conclusions

Direct geoelectrical monitoring of hydraulic exchange with less-mobile porosity has been applied in situ to SWI sediments where redox conditions are expected to show strong spatiotemporal variability. Notable observations from this study include the following:

1. Differential loading of salt tracer was observed within centimeter-scale packets of sand and gravel lakebed sediments at varied location and advective flux rate.
2. Less-mobile porosity fractions were comparable to mobile fractions when the geoelectrical measurements were made adjacent to a cobble obstruction.

3. Anoxic signals (reduced N) were present in all reactive experiments at depths where porewater sampling indicated bulk-oxic conditions.
4. When downward water flux was reduced, the redox transition contracted toward the SWI, and net micro-zone reactivity was enhanced at the shallowest sampling depth.

Less-mobile exchange timescales were extracted semianalytically from paired fluid and bulk EC data, without the need for inverse model calibration and estimated on the order of approximately 45–80 min at lower experimental advective fluxes. This enhanced local residence time seems to induce embedded redox zonation, particularly impacting reactive cycling of nitrate (primary nutrient) and nitrous oxide (strong greenhouse gas). Less-mobile exchange in sand-and-cobble sediments likely results from a spectrum of advective time-scales, as opposed to diffusion-dominated less-mobile exchange such that might be found with clay and peat lenses and is therefore particularly sensitive to variation in flow rate. The new method presented here will allow direct parameterization of reactive SWI models with elusive less-mobile porosity characteristics measured in the field, which can be used to improve the prediction of contaminant transport and greenhouse gas production.

Acknowledgments

We gratefully acknowledge the field help of Rayna Mitzman, Erin Seybold, Danielle Hare, and David Rey. Funding for this project was provided by NSF grants EAR-1446300 and EAR-1446328, the U.S. Geological Survey (USGS) Office of Groundwater, USGS National Research Program, and the USGS Toxic Substances Hydrology Program. Codes for data analysis were developed under Environmental Security Technology Certification Program project ER-201732. Data shown in this paper are publically available as stated in the reference list. Any use of trade, firm, or product names is for descriptive purposes only and does not imply endorsement by the U.S. Government.

References

- Archie, G. E. (1942). The electrical resistivity log as an aid in determining some reservoir characteristics. *Transactions of AIME*, *146*(01), 54–62. <https://doi.org/10.2118/942054-G>
- Bahr, J. M., & Rubin, J. (1987). Direct comparison of kinetic and local equilibrium formulations for solute transport affected by surface reactions. *Water Resources Research*, *23*(3), 438–452. <https://doi.org/10.1029/WR023i003p00438>
- Bajracharya, K., & Barry, D. A. (1997). Nonequilibrium solute transport parameters and their physical significance: Numerical and experimental results. *Journal of Contaminant Hydrology*, *24*(3–4), 185–204. [https://doi.org/10.1016/S0169-7722\(96\)00017-4](https://doi.org/10.1016/S0169-7722(96)00017-4)
- Bardini, L., Boano, F., Cardenas, M. B., Revelli, R., & Ridolfi, L. (2012). Nutrient cycling in bedform induced hyporheic zones. *Geochimica et Cosmochimica Acta*, *84*(January), 47–61. <https://doi.org/10.1016/j.gca.2012.01.025>
- Boano, F., Harvey, J. W., Marion, A., Packman, A. I., Revelli, R., Ridolfi, L., & Worman, A. (2014). Hyporheic flow and transport processes: Mechanisms, models, and biogeochemical implications. *Reviews of Geophysics*, *52*, 603–679. <https://doi.org/10.1002/2012RG000417>
- Briggs, M. A., Day-Lewis, F. D., Ong, J. B. T., Curtis, G. P., & Lane, J. W. (2013). Simultaneous estimation of local-scale and flow path-scale dual-domain mass transfer parameters using geoelectrical monitoring. *Water Resources Research*, *49*, 5615–5630. <https://doi.org/10.1002/wrcr.20397>
- Briggs, M. A., Day-Lewis, F. D., Ong, J. B. T., Harvey, J. W., & Lane, J. W. (2014). Dual-domain mass transfer parameters from electrical hysteresis: Theory and analytical approach applied to laboratory, synthetic streambed, and groundwater experiments. *Water Resources Research*, *50*, 8281–8299. <https://doi.org/10.1002/2014WR015880>
- Briggs, M. A., Day-Lewis, F. D., Scruggs, C., MahmoodPoor Dehkordy, F., Singha, K., & Lane, J. W. (2018). Fluid and bulk electrical conductivity data collected for the study of hydrologic exchange occurring with less-mobile porosity in sandy lakebed sediments: U.S. Geological Survey data release. <https://doi.org/10.5066/F71Z42NF>
- Briggs, M. A., Day-Lewis, F. D., Zarnetske, J. P., & Harvey, J. W. (2015). A physical explanation for the development of redox microzones in hyporheic flow. *Geophysical Research Letters*, *42*, 4402–4410. <https://doi.org/10.1002/2015GL064200>
- Briggs, M. A., Lautz, L. K., & Hare, D. K. (2014). Residence time control on hot moments of net nitrate production and uptake in the hyporheic zone. *Hydrological Processes*, *28*(11), 3741–3751. <https://doi.org/10.1002/hyp.9921>
- Cardenas, M. B. (2004). Impact of heterogeneity, bed forms, and stream curvature on subchannel hyporheic exchange. *Water Resources Research*, *40*, W08307. <https://doi.org/10.1029/2004WR003008>
- Culkin, S. L., Singha, K., & Day-Lewis, F. D. (2008). Implications of rate-limited mass transfer for aquifer storage and recovery. *Ground Water*, *46*(4), 591–605. <https://doi.org/10.1111/j.1745-6584.2008.00435.x>
- Day-Lewis, F. D., Linde, N., Haggerty, R., Singha, K., & Briggs, M. A. (2017). Pore network modeling of the electrical signature of solute transport in dual-domain media. *Geophysical Research Letters*, *44*, 4908–4916. <https://doi.org/10.1002/2017GL073326>
- Day-Lewis, F. D., & Singha, K. (2008). Geoelectrical inference of mass transfer parameters using temporal moments. *Water Resources Research*, *44*, W05201. <https://doi.org/10.1029/2007WR006750>
- Dehkordy, F. M. P., Briggs, M. A., Day-Lewis, F. D., & Bagtzoglou, A. C. (2018). Simulation of less-mobile porosity dynamics in contrasting sediment-water interface porous media. *Hydrological Processes*, *32*, 2030–2043. <https://doi.org/10.1002/hyp.13134>
- Feehley, C. E., Zheng, C., & Molz, F. J. (2000). A dual-domain mass transfer approach for modeling solute transport in heterogeneous aquifers: Application to the Macrodispersion Experiment (MADE) site. *Water Resources Research*, *36*(9), 2501–2515. <https://doi.org/10.1029/2000WR900148>
- Firestone, M. K., & Tiedje, J. M. (1979). Temporal change in nitrous oxide and dinitrogen from denitrification following onset of anaerobiosis. *Applied and Environmental Microbiology*, *38*(4), 673–679.
- Gomez-Velez, J. D., Harvey, J. W., Cardenas, M. B., & Kiel, B. (2015). Denitrification in the Mississippi River network controlled by flow through river bedforms. *Nature Geoscience*, *8*(12), 941–945. <https://doi.org/10.1038/NGEO2567>
- Guan, J., Molz, F. J., Zhou, Q., Liu, H. H., & Zheng, C. (2008). Behavior of the mass transfer coefficient during the MADE-2 experiment: New insights. *Water Resources Research*, *44*, W02423. <https://doi.org/10.1029/2007WR006120>
- Haggerty, R. (2004). What controls the apparent timescale of solute mass transfer in aquifers and soils? A comparison of experimental results. *Water Resources Research*, *40*, W01510. <https://doi.org/10.1029/2002WR001716>
- Haggerty, R., Fleming, S. W., Meigs, L. C., & McKenna, S. A. (2001). Tracer tests in a fractured dolomite 2. Analysis of mass transfer in single-well injection-withdrawal tests. *Water Resources Research*, *37*(5), 1129–1142. <https://doi.org/10.1029/2000WR900334>
- Hare, D. K., Boutt, D. F., Clement, W. P., Hatch, C. E., Davenport, G., & Hackman, A. (2017). Hydrogeological controls on spatial patterns of groundwater discharge in peatlands. *Hydrology and Earth System Sciences*, *21*, 6031–6048. <https://doi.org/10.5194/hess-2017-282>

- Harvey, C. F., & Gorelick, S. M. (2000). Rate-limited mass transfer or macrodispersion: Which dominates plume evolution at the Macrodispersion Experiment (MADE) site? *Water Resources Research*, *36*(3), 637–650. <https://doi.org/10.1029/1999WR900247>
- Harvey, J. W., Böhlke, J. K., Voytek, M. A., Scott, D., & Tobias, C. R. (2013). Hyporheic zone denitrification: Controls on effective reaction depth and contribution to whole-stream mass balance. *Water Resources Research*, *49*, 6298–6316. <https://doi.org/10.1002/wrcr.20492>
- Harvey, J. W., Chambers, R. M., & Hoelscher, J. R. (1995). Preferential flow and segregation of porewater solutes in wetland sediment. *Estuaries*, *18*(4), 568–578. <https://doi.org/10.2307/1352377>
- Hedin, L. O., Von Fischer, J. C., Ostrom, N. E., Kennedy, B. P., Brown, M. G., & Philip Robertson, G. (1998). Thermodynamic constraints on nitrogen transformations and other biogeochemical processes at soil-stream interfaces. *Ecology*, *79*(2), 684–703. <https://doi.org/10.1016/j.jhydrol.2015.10.054>
- Holmes, R., Jones, J., Fisher, S., & Grimm, N. (1996). Denitrification in a nitrogen-limited stream ecosystem. *Biogeochemistry*, *1988*, 125–146.
- Kaufman, M. H., Cardenas, M. B., Buttles, J., Kessler, A. J., & Cook, P. L. M. (2017). Hyporheic hot moments: Dissolved oxygen dynamics in the hyporheic zone in response to surface flow perturbations. *Water Resources Research*, *53*, 6642–6662. <https://doi.org/10.1002/2016WR020296>
- Keery, J., Binley, A., Crook, N., & Smith, J. W. N. (2007). Temporal and spatial variability of groundwater–surface water fluxes: Development and application of an analytical method using temperature time series. *Journal of Hydrology*, *336*(1–2), 1–16. <https://doi.org/10.1016/j.jhydrol.2006.12.003>
- Kessler, A. J., Cardenas, M. B., Santos, I. R., & Cook, P. L. M. (2014). Enhancement of denitrification in permeable carbonate sediment due to intra-granular porosity: A multi-scale modelling analysis. *Geochimica et Cosmochimica Acta*, *141*, 440–453. <https://doi.org/10.1016/j.gca.2014.06.028>
- Lautz, L. K. (2012). Observing temporal patterns of vertical flux through streambed sediments using time-series analysis of temperature records. *Journal of Hydrology*, *464–465*, 199–215. <https://doi.org/10.1016/j.jhydrol.2012.07.006>
- LeBlanc, D. R. (2003). Diffusion and drive-point sampling to detect ordnance-related compounds in shallow ground water beneath Snake Pond, Cape Cod, Massachusetts, 2001–02. *U.S. Geological Survey Water-Resources Investigations Report 03–4133*.
- Li, L., Barry, D. A., Cuiligan-Hensley, P. J., & Bajracharya, K. (1994). Mass transfer in soils with local stratification of hydraulic conductivity. *Water Resources Research*, *30*(11), 2891–2900. <https://doi.org/10.1029/94WR01218>
- Liu, Y., & Kitanidis, P. K. (2012). Applicability of the dual-domain model to nonaggregated porous media. *Ground Water*, *50*(6), 927–934. <https://doi.org/10.1111/j.1745-6584.2011.00909.x>
- Lowry, C. S., Walker, J. F., Hunt, R. J., & Anderson, M. P. (2007). Identifying spatial variability of groundwater discharge in a wetland stream using a distributed temperature sensor. *Water Resources Research*, *43*, W10408. <https://doi.org/10.1029/2007WR006145>
- Ma, R., & Zheng, C. (2011). Not all mass transfer rate coefficients are created equal. *Groundwater*, *49*(6), 772–774. <https://doi.org/10.1111/j.1745-6584.2011.00822.x>
- Marzadri, A., Tonina, D., & Bellin, A. (2012). Morphodynamic controls on redox conditions and on nitrogen dynamics within the hyporheic zone: Application to gravel bed rivers with alternate-bar morphology. *Journal of Geophysical Research*, *117*, G00N10. <https://doi.org/10.1029/2012JG001966>
- Marzadri, A., Tonina, D., Bellin, A., & Tank, J. L. (2014). A hydrologic model demonstrates nitrous oxide emissions depend on streambed morphology. *Geophysical Research Letters*, *41*, 5484–5491. <https://doi.org/10.1002/2014GL060732>
- McKenna, S. A., Meigs, L. C., & Haggerty, R. (2001). Tracer tests in a fractured dolomite 3. Double-porosity, multiple-rate mass transfer processes in convergent flow tracer tests. *Water Resources Research*, *37*(5), 1143–1154. <https://doi.org/10.1029/2000WR900333>
- McWhorter, D. B., & Sunada, D. K. (1977). *Ground-water hydrology and hydraulics*. Fort Collins, CO: Water Resources Publications.
- Menichino, G. T., Ward, A. S., & Hester, E. T. (2014). Macropores as preferential flow paths in meander bends. *Hydrological Processes*, *28*(3), 482–495. <https://doi.org/10.1002/hyp.9573>
- Payn, R. A., Gooseff, M. N., McGlynn, B. L., Bencala, K. E., & Wondzell, S. M. (2009). Channel water balance and exchange with subsurface flow along a mountain headwater stream in Montana, United States. *Water Resources Research*, *45*, W11427. <https://doi.org/10.1029/2008WR007644>
- Quick, A. M., Reeder, W. J., Farrell, T. B., Tonina, D., Feris, K. P., & Benner, S. G. (2016). Controls on nitrous oxide emissions from the hyporheic zones of streams. *Environmental Science and Technology*, *50*(21), 11,491–11,500. <https://doi.org/10.1021/acs.est.6b02680>
- Rosenberry, D. O., Briggs, M. A., Delin, G., & Hare, D. K. (2016). Combined use of thermal methods and seepage meters to efficiently locate, quantify, and monitor focused groundwater discharge to a sand-bed stream. *Water Resources Research*, *52*, 4486–4503. <https://doi.org/10.1002/2016WR018808>
- Rosenberry, D. O., Sheibley, R. W., Cox, S. E., Simonds, F. W., & Naftz, D. L. (2013). Temporal variability of exchange between groundwater and surface water based on high-frequency direct measurements of seepage at the sediment-water interface. *Water Resources Research*, *49*, 2975–2986. <https://doi.org/10.1002/wrcr.20198>
- Sawyer, A. H. (2015). Enhanced removal of groundwater-borne nitrate in heterogeneous aquatic sediments. *Geophysical Research Letters*, *42*, 403–410. <https://doi.org/10.1002/2014GL062234>
- Schmidt, C., Martienssen, M., & Kalbus, E. (2011). Influence of water flux and redox conditions on chlorobenzene concentrations in a contaminated streambed. *Hydrological Processes*, *25*(2), 234–245. <https://doi.org/10.1002/hyp.7839>
- Singha, K., Day-Lewis, F. D., & Lane, J. W. (2007). Geoelectrical evidence of bicontinuum transport in groundwater. *Geophysical Research Letters*, *34*, L12401. <https://doi.org/10.1029/2007GL030019>
- Singha, K., & Gorelick, S. M. (2005). Saline tracer visualized with three-dimensional electrical resistivity tomography: Field-scale spatial moment analysis. *Water Resources Research*, *41*, W05023. <https://doi.org/10.1029/2004WR003460>
- Stewart, R. J., Wollheim, W. M., Gooseff, M. N., Briggs, M. A., Jacobs, J. M., Peterson, B. J., & Hopkinson, C. S. (2011). Separation of river network-scale nitrogen removal among the main channel and two transient storage compartments. *Water Resources Research*, *47*, W00J10. <https://doi.org/10.1029/2010WR009896>
- Stoliker, D. L., Repert, D. A., Smith, R. L., Song, B., Leblanc, D. R., McCobb, T. D., et al. (2016). Hydrologic controls on nitrogen cycling processes and functional gene abundance in sediments of a groundwater flow-through lake. *Environmental Science & Technology*, *50*(7), 3649–3657. <https://doi.org/10.1021/acs.est.5b06155>
- Swanson, R. D., Singha, K., Day-lewis, F. D., Binley, A., Keating, K., & Haggerty, R. (2012). Direct geoelectrical evidence of mass transfer at the laboratory scale. *Water Resources Research*, *48*, W10543. <https://doi.org/10.1029/2012WR012431>
- Toran, L., Nyquist, J. E., Fang, A. C., Ryan, R. J., & Rosenberry, D. O. (2013). Observing lingering hyporheic storage using electrical resistivity: Variations around stream restoration structures, Crabby Creek, PA. *Hydrological Processes*, *27*(10), 1411–1425. <https://doi.org/10.1002/hyp.9269>

- Triska, F. J., Duff, J. H., & Avanzino, R. J. (1993). The role of water exchange between a stream channel and its hyporheic zone in nitrogen cycling at the terrestrial-aquatic interface. *Hydrobiologia*, 251(1–3), 167–184. <https://doi.org/10.1007/BF00007177>
- van Genuchten, M. T., & Wierenga, P. J. (1976). Mass transfer studies in sorbing porous media I. Analytical solutions. *Soil Science Society of America Journal*, 40(4), 473–480. <https://doi.org/10.2136/sssaj1976.03615995004000040011x>
- Wagner, B. J., & Harvey, J. W. (1997). Experimental design for estimating parameters of rate-limited mass transfer: Analysis of stream tracer studies. *Water Resources Research*, 33(7), 1731–1741. <https://doi.org/10.1029/97WR01067>
- Walter, B. D. A., & Masterson, J. P. (2002). Simulated pond-aquifer interactions under natural and stressed conditions near Snake Pond, Cape Cod. U.S. Geological Survey Water-Resources Investigations Report 99-4174, 34.
- Ward, A. S., Gooseff, M. N., & Singha, K. (2010). Imaging hyporheic zone solute transport using electrical resistivity. *Hydrological Processes*, 24(7), 948–953. <https://doi.org/10.1002/hyp.7672>
- Wheaton, D. D., & Singha, K. (2010). Investigating the impact of advective and diffusive controls in solute transport on geoelectrical data. *Journal of Applied Geophysics*, 72(1), 10–19. <https://doi.org/10.1016/j.jappgeo.2010.06.006>
- Winter, T. C., Harvey, J. W., Franke, O. L., & Alley, W. M. (1998). Ground water and surface water; a single resource. *U. S. Geological Survey Circular*, 1139, 79.
- Wondzell, S. M. (2011). The role of the hyporheic zone across stream networks. *Hydrological Processes*, 25(22), 3525–3532. <https://doi.org/10.1002/hyp.8119>
- Wondzell, S. M. (2015). Groundwater-surface-water interactions: Perspectives on the development of the science over the last 20 years. *Freshwater Science*, 34(1), 368–376. <https://doi.org/10.1086/679665>
- Zarnetske, J. P., Haggerty, R., Wondzell, S. M., & Baker, M. a. (2011). Dynamics of nitrate production and removal as a function of residence time in the hyporheic zone. *Journal of Geophysical Research*, 116, G01025. <https://doi.org/10.1029/2010JG001356>
- Zarnetske, J. P., Haggerty, R., Wondzell, S. M., Bokil, V. A., & González-Pinzón, R. (2012). Coupled transport and reaction kinetics control the nitrate source-sink function of hyporheic zones. *Water Resources Research*, 48, W11508. <https://doi.org/10.1029/2012WR011894>
- Zheng, C., & Wang, P. P. (1999). *MT3DMS: A modular three-dimensional multi-species model for simulation of advection, dispersion and chemical reactions of contaminants in groundwater systems: Documentation and user's guide. SERDP-99-1*. Vicksburg, MS: US Army Engineer Research and Development Center.
- Zinn, B., & Harvey, C. F. (2003). When good statistical models of aquifer heterogeneity go bad: A comparison of flow, dispersion, and mass transfer in connected and multivariate Gaussian hydraulic conductivity fields. *Water Resources Research*, 39(3), 1051. <https://doi.org/10.1029/2001WR001146>